Orientation-dependent high-order harmonic generation in HCN: Insights from time-dependent density-functional-theory calculations

Xi Chu ●

Department of Chemistry and Biochemistry, The University of Montana, Missoula, Montana 59812, USA

This study examines the orientation-dependent high-order harmonic spectra of HCN, using time-dependent density-functional-theory calculations. In HCN, which lacks inversion symmetry, the emergence of even harmonics is a notable feature. At a parallel orientation to the laser polarization, these even harmonics manifest with intensities surpassing those of odd harmonics. However, their magnitudes diminish as the orientation shifts away from parallel. Conversely, at a perpendicular orientation to the laser polarization, the spectrum predominantly displays odd harmonics, although an exclusively even harmonic spectrum is generated with the harmonic polarization perpendicular to the laser. The intensities of these even harmonics wane as the molecular orientation deviates from the perpendicular. The behavior of odd harmonics is more intricate, generally showing heightened intensities at perpendicular orientations. The influence of laser parameters on the orientation dependence is minimal. Across various orientations and laser settings, a consistent minimum is observed near 22–23 eV, underscoring a universal feature of the high-order harmonic spectra of HCN. Regardless of the orientation, the highest occupied molecular orbitals (HOMOs) contribute little to the high-order even harmonics. As far as the high-order odd harmonics are concerned, the HOMOs only dominate when the orientation angle is greater than $30°$.

I. INTRODUCTION

High-order harmonic generation (HHG) in noncentrosymmetric media, such as aligned polar molecules, displays an asymmetry for opposite orientations of the molecular dipole moment relative to the laser polarization [1–4]. This asymmetry is pivotal in generating even harmonics. The analysis of even versus odd harmonics allows for imaging asymmetric molecular orbitals [5]. The even-to-odd intensity ratio, tunable by molecular orientation in intense linearly polarized fields, can be employed in detecting transient electronic structures [6].

The dependence of even harmonics on molecular orientation provides insights into the degree of orientation [4,7] and rotational dynamics [4]. Additionally, the correlation between even-odd harmonics and ultrafast nuclear dynamics has been established [8], extending to systems like biased bilayer graphene [9].

In molecules lacking inversion symmetry, asymmetry influences various aspects of their high-order harmonic spectra when rescattering is oriented, including two-center interference and ellipticity [10,11]. The analysis of even-odd harmonics has been instrumental in understanding isotope effects [12], shape resonance [13], and charge migration [14].

The three-step model, involving tunneling, propagation, and recombination of an active electron from the highest occupied molecular orbital (HOMO), frames the HHG process [15,16]. In polar molecules, the recombining electron interacts with the molecule's electric dipole moment in addition to the laser field, a phenomenon absent in nonpolar molecules.

In experimental setups for molecular frame measurements, a common approach involves employing a weaker field to dynamically align [17] or orient [18] the molecules, followed by applying an intense field to generate high-order harmonic radiation. In addition to the single molecule response, it is essential to model the alignment and orientation distribution [11,19] of the molecules and the macroscopic response encompassing the propagation of the harmonics through the ensemble of molecules [20,21] to replicate experimental observations. Successful comparisons between experiments and theory have been made at the level of the quantitative rescattering model [19] and time-dependent density functional theory (TDDFT) [22] for both polar and nonpolar molecules concerning two-center interference minima.

In this work, we focus on the single molecule HHG spectra of HCN for its substantial dipole moment exceeding that of other studied polar molecules like $HeH_2{}^+$, CO, and NO. Therefore, it is a prime candidate for observing high-order even harmonic intensities.

When the molecular dipole moment is misaligned with the laser field, the direction of the recombination dipole deviates from the laser polarization, leading to the generation of even harmonics perpendicular to the laser polarization, as reported of CO [23]. The significant dipole moment of HCN suggests a more pronounced effect. This study compares harmonic intensities with polarizations perpendicular and parallel to the driving field using TDDFT calculations.

HCN's ground state ($X\,^1\Sigma^+$) electron configuration is $1\sigma^2 2\sigma^2 3\sigma^2 4\sigma^2 5\sigma^2 1\pi^4$. The similar ionization potentials to the cation states $X\,^2\Pi\,(1\pi^{-1})$ and $A\,^2\Sigma^+\,(5\sigma^{-1})$ [24] suggest potential involvement of both states in rescattering. The

tautomer HNC, with its similar vertical ionization potentials to the two lowest cation states, also presents an intriguing case for study. Despite HNC being a zwitterion and less abundant on Earth due to its higher energy, the process of isomerization from HCN to HNC holds significant interest, particularly in astrophysics. HHG spectra along the isomerization reaction path from HCN to HNC were calculated using the Lewenstein model, aiming to establish a correlation between spectral intensity and stationary points on the reaction coordinates [25].

Addressing multiorbital involvement [26–30], many-electron effects [31–33], interference [28,34–36], and resonances [28,37,38], TDDFT methods [39] are often employed in HHG calculations, including those for asymmetric molecules [6,11,23,40]. TDDFT calculations indicate substantial contributions from σ orbitals, despite 1π being the HOMO of HCN [41,42].

When the laser polarization aligns with the molecular axis, multiple molecular orbital involvement induces a cancellation effect, reducing odd harmonics in the plateau. A minimum for odd harmonics is attributed to interference of different contributions [42]. Meanwhile, the near-cutoff harmonics are dominated by σ contributions [42].

This work employs TDDFT to investigate how HCN's high-order harmonic spectral features depend on the molecular orientation angle relative to the laser field. We analyze the variation of odd and even harmonic intensities near threshold, in the plateau, at a minimum, and at cutoff with orientation, highlighting the effects of a significant dipole moment on the high-order harmonic spectrum.

II. THEORY AND METHOD

We solve the time-dependent (TD) Kohn-Sham (KS) equations:

$$i\hbar \frac{\partial}{\partial t}\psi_j(\boldsymbol{r}, t)$$
$$= [\hat{H}^{(0)}(\boldsymbol{r}) + \Delta v(\boldsymbol{r}, t) + e\boldsymbol{E}(t)\cdot\boldsymbol{r}]\psi_j(\boldsymbol{r}, t), \quad (1)$$

where j represents the spin-orbital index, $\boldsymbol{r}$ is the spatial coordinate, t is time, $\hat{H}^{(0)}$ is the field-free Hamiltonian, $\boldsymbol{E}$ is the laser's electric field, and Δv is the induced potential. The TD electron density $\rho(\boldsymbol{r}, t)$ is computed as

$$\rho(\boldsymbol{r}, t) = \sum_{i=1}^{N} \psi_i^*(\boldsymbol{r}, t)\psi_i(\boldsymbol{r}, t), \quad (2)$$

with $N = 14$ representing the number of electrons.

We determine the initial state, prior to the application of the external field, by solving the static KS equation with an LB_α exchange-correlation potential [43,44]:

$$\hat{H}^{(0)}(\boldsymbol{r})\psi_j(\boldsymbol{r}, 0) = \epsilon_j\psi_j(\boldsymbol{r}, 0), \quad j = 1, 2, \ldots, N. \quad (3)$$

A generalized pseudospectral method [45,46] is adopted with a 3D grid consisting of 30 planes containing the molecular axis. We use 9600 unevenly distributed grid points per plane. The grid points are denser near the nuclei. The maximum distance to the nuclear charge center is $r_{\max} = 300a_0$. The chosen $r_{\max}$ is sufficiently large to ensure the proper representation of the free-electron wave functions and energies, which are subject to the same $\hat{H}^{(0)}(\boldsymbol{r})$.

TABLE I. Orbital energies (ϵ) of HCN and the ground-state occupation. All energies are in eV. The C-N distance is $2.184a_0$ [47] and the H-C distance is $2.011a_0$ [47]. The calculated electric dipole moment is 3.084 D, consistent with the experimental value of 2.93 D [48].

Orb.	ϵ	occ.	I_p	excitation	$\Delta\epsilon$	Energy
1γ	−0.703	0				
1δ	−1.212	0				
6σ	−4.128	0		$4\sigma \to 6\sigma$	15.458	16.6 [24]
2π	−5.793	0		$4\sigma \to 2\pi$	13.793	15.2 [24]
1π	−13.617	4	13.607 [24]			
5σ	−13.764	4	14.011 [24]			
4σ	−19.586	4	19.06 [49]			
3σ	−27.307	2				

Orbital energies and ground-state occupations for HCN are tabulated in Table I, compared against experimental vertical ionization potentials. The agreement between the negative of our calculated energies and the measured ionization potentials is satisfactory. The orbital energy differences between two unoccupied (2π, 6σ) orbitals and HOMO-2 (4σ) are compared to experimental values of excitation energies as well in Table I. The differences are 1.4 and 1.1 eV, respectively. The measured values for removing an electron from the HOMO (1π) and HOMO-1 (5σ) differ only by 0.4 eV [24], suggesting the potential involvement of both orbitals in an HHG process.

In our simulations, we define the molecular orientation angle α as the angle between the molecular axis and laser polarization. We rotate the molecule about the y axis, keeping the y coordinate constant during the rotation. The polarization of the incident laser is along the z axis, modeled as

$$E(t) = f(t)\sin\omega_0 t, \quad (4)$$

with ω_0 as the angular frequency and $f(t)$ as the envelope of the field strength given by

$$f(t) = F\sin^2\frac{\omega_0 t}{40}, \quad 0 \leqslant t \leqslant 20T, \quad (5)$$

where T denotes an optical cycle.

The initial electron densities of four occupied orbitals for $\alpha = 45°$ are presented on the x-z plane at $y = 0$ in Fig. 1. The HOMO comprises degenerate $1\pi_x$ and $1\pi_y$ orbitals, with the density of $1\pi_x$ shown and that of $1\pi_y$ equaling zero at $y = 0$.

The TD orbitals are propagated using a split-operator method [46], with a time step of 2.419 attoseconds. The Fourier transform of the induced dipole moments is converged to the fourth decimal place at harmonics of the incident light.

We have implemented an absorbing boundary located at $r_0 = 120a_0$ from the nuclear charge center to prevent spurious reflections from the outer boundary. This approach allows for filtering the electron wave packet reaching the edge, $r_{\max}$, thus mimicking ionization. The calculated high-order harmonic intensities are insensitive to the form and parameters of the absorbing functions provided that r_0 is sufficiently distant [45]. The specific absorbing function employed is $\cos^{1/4}[\pi(r - r_0)/2(r_{\max} - r_0)]$ for $r \geqslant r_0$.
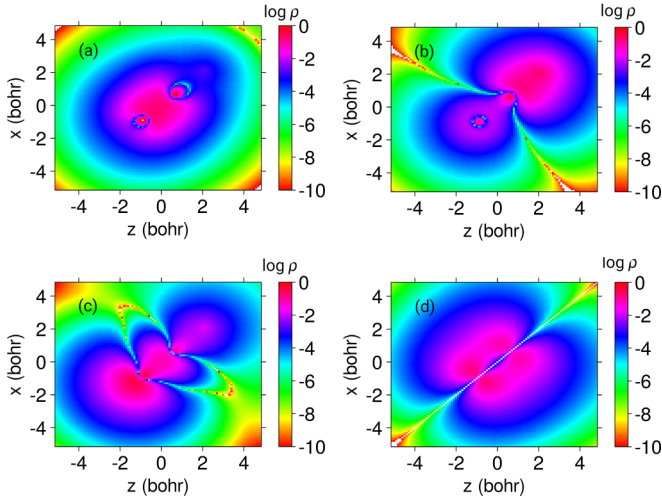
FIG. 1. Electron density [logarithmic scale of $\log_{10}(\rho)$] for occupied orbitals of HCN: (a) 3σ, (b) 4σ, (c) 5σ, and (d) $1\pi_x$. The Cartesian coordinates of N, C, and H are $(-0.874a_0, 0, -0.874a_0)$, $(0.671a_0, 0, 0.671a_0)$, and $(2.092a_0, 0, 2.092a_0)$, respectively.

Setting the nuclear charge center as the origin of coordinates and thus neutralizing the nuclear contribution to the dipole moment, the TD dipole moment is calculated from the electron density as

$$d_p(t) = -e \int \int \int \rho(\mathbf{r}, t) p d^3 \mathbf{r}, \tag{6}$$

with $p = z$ or x and converted from the dipole acceleration as well. The HHG power spectrum is presented as $|d_p(\omega)|^2$ and

$$d(\omega)_p = \frac{1}{t_f - t_i} \int_{t_i}^{t_f} d_p(t) e^{-i\omega t} dt, \tag{7}$$

with $t_i = 0$ and $t_f = 20T$.

III. RESULTS

A. Basic symmetries in the HHG spectra of an oriented molecule

The TD dipole moment for parallel ($\alpha = 0°$) and perpendicular ($\alpha = 90°$) orientations is illustrated in Fig. 2(a). At $\alpha = 0$, the initial dipole moment is $1.213ea_0$, aligning with the measured molecular dipole moment [48]. The oscillation amplitudes in this orientation exceed those at $\alpha = 90°$, where the induced dipole moment direction deviates slightly from the laser field's.

For the perpendicular orientation, the induced dipole moment includes both x- and z-components, with the molecular axis parallel to the x-axis and the laser polarization along the z-axis. The z-component's oscillation is in sync with the laser frequency, while the x-component oscillates at twice the laser frequency. This indicates that only even harmonics are permitted in the x direction. To enhance visibility, we have amplified the x-component's oscillation amplitudes by a factor of 200.

Due to the axial symmetry of the molecule, both even and odd harmonics in the perpendicular direction (x-polarization) are zero when $\alpha = 0°$ or $180°$. Conversely, when $\alpha = 90°$ or $270°$, even harmonics in the parallel direction
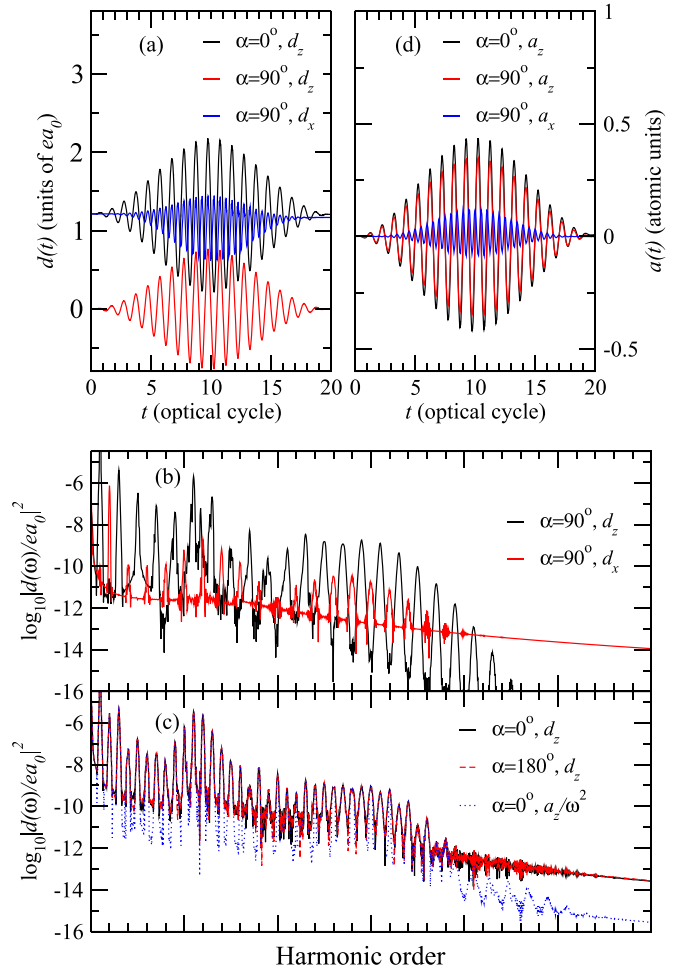

FIG. 2. (a) TDDFT calculated induced dipole moments of HCN at equilibrium geometry, for parallel ($\alpha = 0°$) and perpendicular ($\alpha = 90°$) molecular orientations. The laser, with a wavelength of $\lambda = 1064$ nm and a pulse duration of 20 optical cycles, is linearly polarized along the z-axis at an intensity of 8×10^{13} W/cm^2. (b) HHG spectra for x- and z-polarizations in the perpendicular orientation. (c) Comparison of HHG spectra in parallel and antiparallel orientations, showcasing the spectra for parallel orientation in both length and acceleration gauges. (d) Induced dipole accelerations for parallel ($\alpha = 0°$) and perpendicular ($\alpha = 90°$) molecular orientations. In (a) and (d), the oscillation amplitudes of the blue curves are amplified by a factor of 200.

(z-polarization) and odd harmonics in the perpendicular direction (x-polarization) are forbidden. At other orientation angles, both even and odd harmonics of x- and z-polarization vary with the orientation.

In Fig. 2(b), the HHG spectra for the perpendicular orientation are presented, separating the x and z components of the harmonic polarization. The z component exhibits only odd harmonics, while the x component contains exclusively even harmonics. The intensities of the z component are orders of magnitude higher than those of the x component. In measurements where parallel and perpendicular components of harmonic polarization are not separated, even harmonics with weak intensities are anticipated for $90°$ orientation.
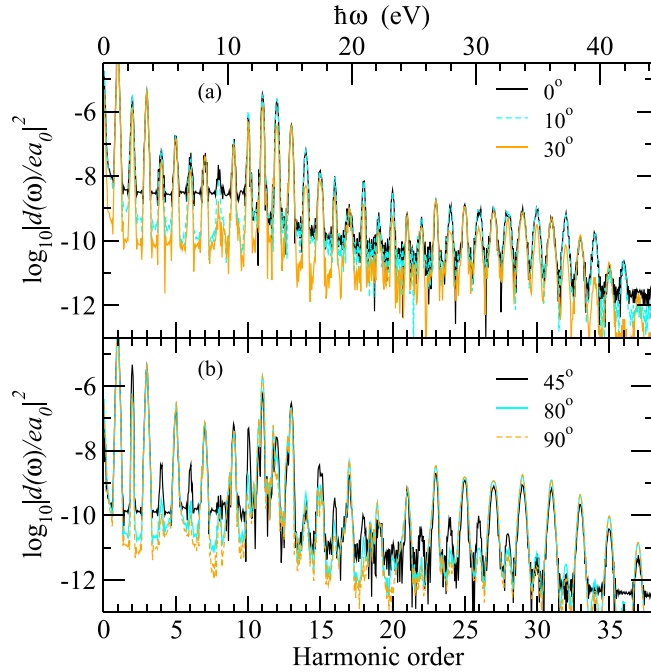
FIG. 3. HHG spectra of HCN calculated for various orientations under 1064 nm linearly polarized $\sin^2$ laser pulses, spanning 20 optical cycles. The intensity is set at $I = 8 \times 10^{13} \, \text{W/cm}^2$, with both the laser and harmonic polarization aligned along the z direction. The specific molecular orientation angles are detailed within the figure legends.

In the following subsections, the harmonic intensities are presented as the sum of the parallel and perpendicular polarization components, i.e.,

$$|d(\omega)|^2 = |d_z(\omega)|^2 + |d_x(\omega)|^2. \qquad (8)$$

Figure 2(c) demonstrates that the spectra for parallel ($\alpha = 0°$) and antiparallel ($\alpha = 180°$) orientations are indistinguishable. In fact, our calculations show that spectra for any orientation angle α, $180° \pm \alpha$, and $360° - \alpha$ are similar.

Additionally, we compare spectra obtained using both the length and acceleration gauges. The only notable difference is the lower baseline in the spectra from acceleration calculations, consistent across all spectra in this study. This consistency serves as a validation of our numerical results.

B. Orientation dependence of an HHG spectrum

The HHG spectra for various orientations of HCN are compared in Fig. 3. In Fig. 3(a), the spectra for orientations at $\alpha = 0°$ and $10°$ are nearly indistinguishable on a logarithmic scale, featuring both even and odd harmonics. The most pronounced peak is at H11, close to the ionization threshold. Below this threshold, even harmonics generally have lower intensities than the odd ones next to them. However, from 19 eV (H16) to 25 eV (H21), odd harmonics are markedly fainter compared to even ones. In the plateau region, between H23 (26.8 eV) and H32 (37.3 eV), even and odd harmonics are similar in intensity.

At $\alpha = 30°$, many harmonic peaks, particularly even ones, are significantly reduced compared to the parallel orientation. Notably, the near-cutoff harmonics H34 (39.6 eV) and H36
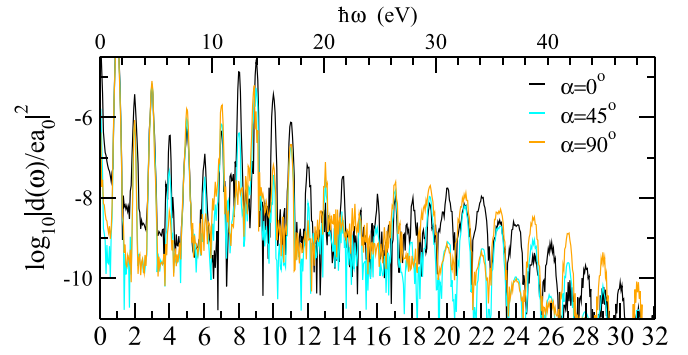
are more than an order of magnitude lower at this angle. For $\alpha = 45°$ [Fig. 3(b)], both H34 and H36 are over two orders of magnitude lower than adjacent odd harmonics, merging into the baseline.

For $\alpha = 80°$ [Fig. 3(b)], even harmonics are almost imperceptible except for H2, H12, and H14. Here, H12 is near the threshold, shifted to $11.7\omega_0$ (13.6 eV). The odd harmonics at this orientation closely resemble those at $\alpha = 90°$. Interestingly, the baseline for the perpendicular orientation is significantly lower, with no even harmonics except for H12, which is near the ionization potential of 13.6 eV. Similar to the parallel orientation, H17 and H19 appear as minima, with peaks being split.

The spectra at $\alpha = 45°$ show substantial differences compared to the parallel or perpendicular orientations. In the plateau between H16 and H21, even harmonics are so diminished that odd ones appear predominant. While H19 remains a minimum for odd harmonics across all orientations, H20 (23.3 eV) is further reduced, over two orders of magnitude lower than in the parallel orientation. Beyond H20, even and odd harmonics exhibit stark differences in intensities, plateau lengths, and cutoff positions.

We performed calculations with different laser wavelengths and intensities, with some spectra presented in Fig. 4. For three representative orientations, the spectral characteristics align with those observed in Fig. 3. The highest peak for all orientations is H9, at 14 eV near the ionization threshold. For the parallel orientation, a notable trend in the even-to-odd intensity ratio emerges below the ionization potential, with H2, H4, and H6 showing significantly lower intensities than H1, H3, H5, and H7.

The contrast between even and odd harmonics is pronounced between H12 (19 eV) and H16 (25 eV). H13 (20.4 eV) is notably lower than H12 or H14, while H15 (23.2 eV) is 14 times less intense than H14 and 5 times less than H16.

The classical cutoff is at 32.5 eV (H21), up to which the harmonic intensities for $\alpha = 45°$ are generally reduced compared to parallel orientations, with the exceptions being odd harmonics H3, H5, H7, H13, and H17. Even harmonics, particularly high-energy ones, are significantly diminished, reduced by two orders of magnitude.

FIG. 4. HHG spectra of HCN at selected orientations under 800 nm linearly polarized $\sin^2$ laser pulses, 20 optical cycles, intensity $10^{14} \, \text{W/cm}^2$. Laser and harmonic polarization are in the z direction, with molecular orientation angles in the legends.
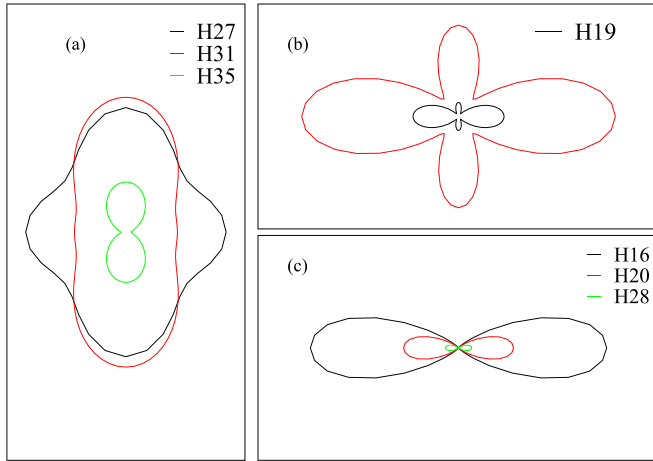
FIG. 5. Polar diagram depicting the angular dependence of harmonic intensity, focusing on (a) odd harmonics in the plateau and near the cutoff, (b) odd harmonics near the ionization threshold and at a global minimum, and (c) even harmonics. High-order harmonics are generated in a 20 optical-cycle $\sin^2$ pulse with an intensity of $I = 8 \times 10^{13}$ W/cm^2 and a wavelength of $\lambda = 1064$ nm. The radial coordinate represents the intensity, and α is the polar angle.

For the perpendicular orientation, only odd harmonics are significant in the spectrum. Most are more intense than in the parallel orientation, except for H9, H11, and H15, with H9 near the ionization threshold and H15 at a minimum. These harmonics also exhibit a redshift. Dismissable even harmonics are exclusively from the x (perpendicular) components. Both the z and x components exhibit a common minimum near 23 eV (H15, H16).

C. Orientation dependence of odd-even harmonics

In Fig. 5, we depict the orientation angle's impact on the intensity of a specific harmonic. H35 (40.8 eV), close to the classical cutoff (40.4 eV), is the extrapolated odd harmonic cutoff from the exponential decay pattern in the HHG spectra. As shown in Fig. 5(a), odd harmonics in the plateau up to the cutoff exhibit a common trend: their intensity peaks at the perpendicular orientation.

For the parallel or antiparallel orientations, the intensity of H27 remains significant, retaining 80% of the intensity compared to the perpendicular orientation. The orientation that yields the lowest intensity for H27 is at $\alpha = 40°$, at 64% of the perpendicular intensity.

In the case of H31, the parallel orientation intensity drops to 38% of the perpendicular orientation. Its intensity is comparable to the lowest observed at $\alpha = 15°$. For H35, the parallel orientation intensity falls to the lowest, merely 10% of the perpendicular orientation.

Figure 5(b) highlights odd harmonics that deviate from the typical pattern of highest intensity at the perpendicular orientation. H11 is near the ionization threshold, while H19 is identified as a spectral minimum.

The pattern for even harmonics in the plateau, as shown in Fig. 5(c), is consistent across the board. Even harmonics near the cutoff are particularly sensitive to orientation deviations beyond 10° from the parallel orientation.
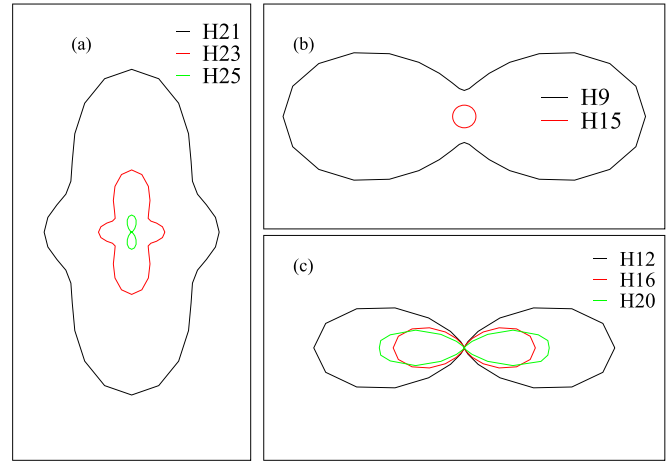
FIG. 6. Polar diagram depicting the angular dependence of the harmonic intensity of (a) odd harmonics in the plateau and near the cutoff, (b) odd harmonics near ionization threshold and at a global minimum, and (c) even harmonics. High-order harmonics are generated in a 20 optical-cycle $\sin^2$ pulse with intensity 10^{14} W/cm^2 and wavelength $\lambda = 800$ nm. The radial coordinate represents the intensity, and α is the polar angle.

Figure 6 presents the angular dependence of selected harmonics, similar in energy to those in Fig. 5. Consistent with Fig. 5(a), the intensities of odd harmonics from the plateau to the cutoff in Fig. 6(a) are highest when the molecular axis is perpendicular to the laser polarization. The lowest intensity occurs at an angle between parallel and perpendicular, approaching $\alpha = 0°$ as the harmonic order increases, with the near-cutoff harmonic H25's intensity being the lowest at $\alpha = 0°$.

Figure 6(b) illustrates the odd harmonics near the threshold (H9) and at the minimum (H15). Their profiles differ from those in Fig. 5(b), although both figures show distinct patterns from other odd harmonics. Similar to Fig. 5(b), the highest intensities are not at the perpendicular orientation but rather at the parallel orientation.

Multiphoton resonances between the ground and Rydberg states play an important role in the enhanced harmonic intensity near the threshold [42]. Concerning resonances, the photon energy is important. Therefore, different wavelengths of lasers lead to varied orientation-dependent intensities.

Regarding the spectral minimum, splitting and shifting occur at H15 in Fig. 4 and at H19 in Fig. 3. In other words, the spectral peak near the minimum is not well defined at an odd harmonic order. In Figs. 6(b) and 5(b), we analyze the intensities at the exact odd harmonic orders. The splitting and shifting thus influence and alter the orientation dependence of these depicted harmonics.

The even harmonics in Fig. 6(c) display an angular distribution very similar to those in Fig. 5(c). The highest intensity occurs at the parallel orientation and rapidly decreases once the angle exceeds 10°.

D. Spectrum of randomly oriented molecules

To obtain the expectation value of a single molecule response within an ensemble of randomly oriented, unaligned molecules, we employ the coherent sum of responses as
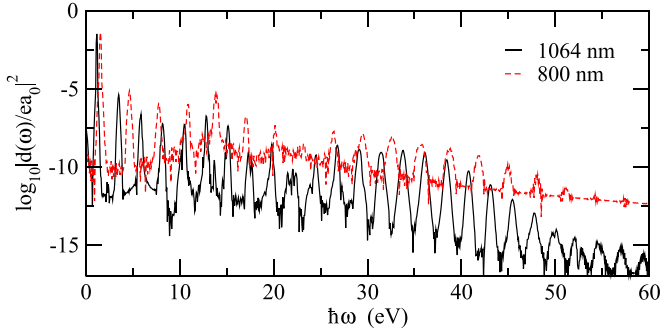
FIG. 7. High-order harmonic spectra of randomly oriented HCN molecules in linearly polarized laser pulses of 8×10^{13} W/cm^2 at 1064 nm and 10^{14} W/cm^2 at 800 nm, respectively, over 20 optical cycles with a sin^2 envelope.

follows:

$$|\langle d(\omega) \rangle|^2 = \left| \frac{1}{2} \int_0^\pi d_z(\omega; \alpha) \sin \alpha \, d\alpha \right|^2$$

$$+ \left| \frac{1}{2} \int_0^\pi d_x(\omega; \alpha) \sin \alpha \, d\alpha \right|^2. \qquad (9)$$

The HHG spectra evaluated with Eq. (9) are given in Fig. 7. In these spectra, the coherent summation leads to the cancellation of all even harmonics, attributing to the loss of asymmetry due to random orientation. The spectra resemble those obtained for the perpendicular orientation but with slightly lower harmonic intensities. Both spectra exhibit a minimum in the 22–23 eV range.

An additional factor of angular distribution function matching experimental conditions needs to be introduced to derive the spectrum corresponding to oriented molecules. Previous studies have demonstrated that the position of the two-center interference minimum in CO$_2$ depends on how tight the molecular alignment is. On the contrary, the spectral minimum of HCN remains unshifted across various degrees of alignment when we experiment with it numerically.

E. Contributions of TD orbitals to the high-order harmonic spectrum

It has been shown that for recombination dipole matrix elements to accurately describe the two-center interference minimum, the transient polarization of the molecular orbital has to be adequately accounted for [50,51]. In a process dominated by the HOMO, the TD orbital obtained in a TDDFT calculation can describe such polarization effects, which are important in the case of OCS [11]. In the case of HCN, further complications derive from the involvement of multiple orbitals.

It is apparent for the parallel or antiparallel orientation that polarization of the HOMO, a π orbital, along the molecular axis does not affect the nodal plane which contains the molecular axis. Transient dynamics of the electron density along the molecular axis are attributed to the σ orbitals.

TDDFT methods enable the calculation of TD orbital densities, given by

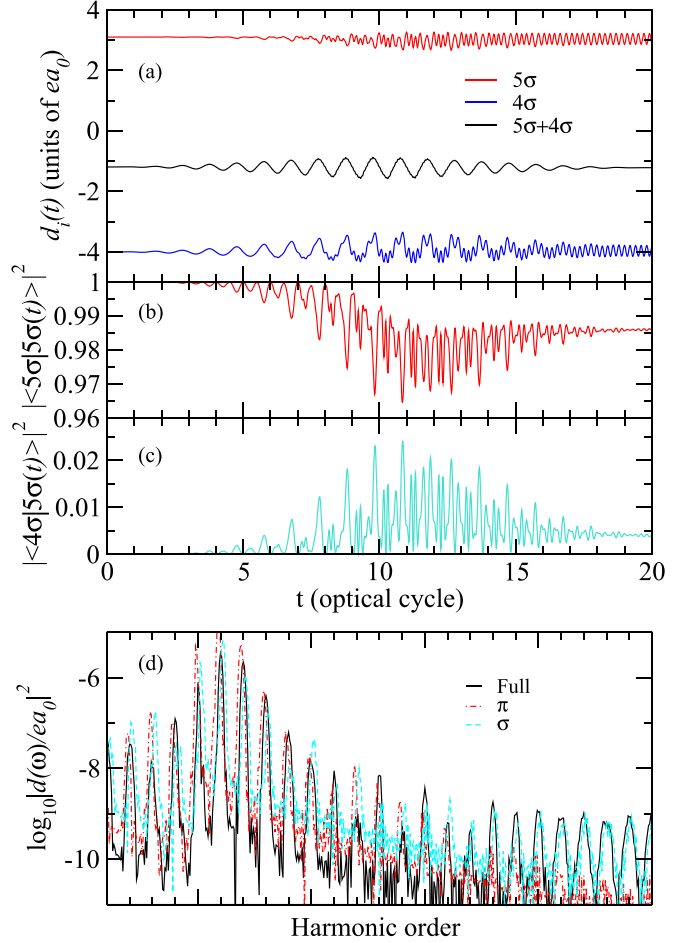$$\rho_i(\mathbf{r}, t) = \psi_i^*(\mathbf{r}, t) \psi_i(\mathbf{r}, t), \qquad (10)$$

FIG. 8. HCN in a laser field of 8×10^{13} W/cm^2 and 1064 nm wavelength, at $\alpha = 0$: (a) Contributions of TD 5σ and 4σ orbitals to the transient dipole moment. (b) Projection of TD 5σ onto field-free 5σ. (c) Projection of TD 5σ onto field-free 4σ. (d) Contributions of σ and π orbitals to the high-order harmonic spectrum.

which provides insights into the contributions of orbitals to the HHG process through

$$d_{i,p}(t) = -e \langle \psi_i(\mathbf{r}, t) | p | \psi_i(\mathbf{r}, t) \rangle, \qquad (11)$$

and its frequency domain representation:

$$d_{i,p}(\omega) = \frac{1}{t_f - t_i} \int_{t_i}^{t_f} d_i(t) e^{-i\omega t} dt \qquad (12)$$

and $|d(\omega)|^2 = |d_{i,z}(\omega)|^2 + |d_{i,x}(\omega)|^2$.

To associate these TD orbitals with a recombination matrix element, however, it is important to note that the TDKS orbitals are not always physically meaningful. Figure 8(a) demonstrates the contributions of the TD 5σ and 4σ orbitals to the dipole moment. These contributions do not mimic the form of $E(t)$ as observed in the total induced dipole moment [see Fig. 2(a)]. Intriguingly, both orbitals exhibit oscillations as the field approaches zero, yet these oscillations are canceled when their contributions are combined.

We also investigate the TD 5σ orbital's projection onto the field-free 5σ and 4σ orbitals, as displayed in Figs. 8(b) and 8(c). The results reveal that a minor portion of the transient
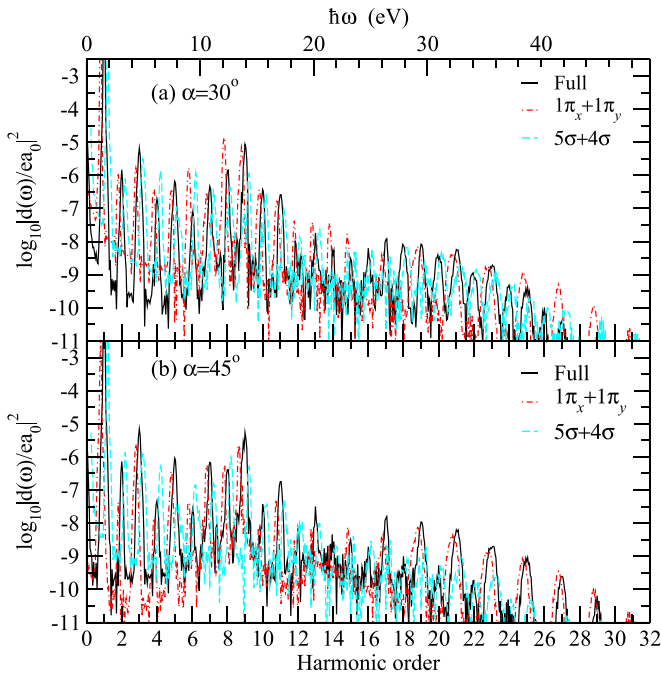
FIG. 9. Orbital contributions to the high-order harmonic spectrum of HCN oriented at $\alpha = 30°$ and $45°$ in a laser field of 10^{14} W/cm^2 and 800 nm wavelength. The TD$1\pi_x + 1\pi_y$ orbitals are shifted to the left slightly, and those of the TD$5\sigma + 4\sigma$ are shifted to the right.

FIG. 10. Orbital contributions to the high-order harmonic spectrum of HCN in a laser field of 10^{14} W/cm^2 and 800 nm wavelength for $\alpha = 90°$.

orbital density is composed of the field-free 4σ component, persisting even after the field ceases. Similarly, the TD 4σ orbital (not depicted) contains a component of the field-free 5σ orbital.

Essentially, these two TD orbitals exchange a fraction of their populations in the presence of the field. This exchange, however, does not impact the total TD electron density, which forms the basis for observables like the transient dipole moment and the harmonic spectrum. Consequently, the misleading interpretation of population exchange results from segregating the TD density into orbital contributions.

In orientations parallel or antiparallel to the laser, the magnetic quantum number m remains conserved. This conservation allows for a distinct separation of contributions from σ ($m = 0$) and π ($m = 1$, HOMO) orbitals, as illustrated in Fig. 8(d). In this figure, we take the coherent sum of TD 5σ and 4σ contributions, and the baseline is reduced. It is apparent that the σ contributions are far more significant when the harmonic energy is higher than 25 eV.

The m quantum number is no longer conserved when orientations deviate from parallel or antiparallel. However, the spurious population exchange still requires the coherent sum of TD 5σ and 4σ to account for orbital contributions properly. In Fig. 9, we present such combined contributions.

The contribution of the HOMOs to the odd high-order harmonics increases with the orientation angle. It dominates at $30°$ orientation and exclusively dominates at $45°$ orientation. Specifically, $1\pi_x$ and $1\pi_y$ both contribute significantly to the odd high-order harmonics at $\alpha = 30°$ and $1\pi_x$ dominates exclusively at $\alpha = 45°$ and above. For the even harmonics, on the other hand, the HOMOs only contribute to those below
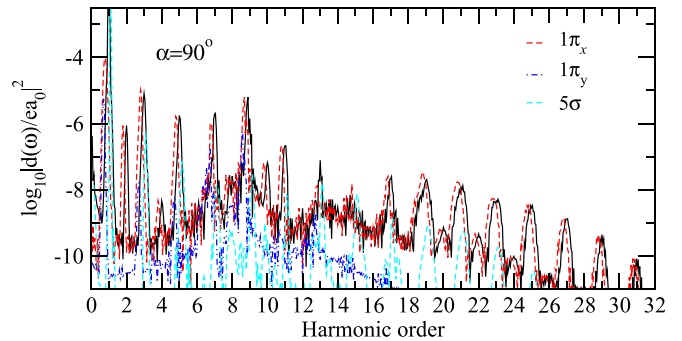
25 eV. Even high-order harmonics above 25 eV are generated by the σ orbitals.

For the perpendicular orientation, the population exchange between HOMO-1 and HOMO-2 is forbidden by symmetry. Therefore, we present the contributions of 5σ and 4σ separately in Fig. 10. The HOMO ($1\pi_x$) dominates, and $1\pi_y$ contributes significantly only near the ionization threshold. The HOMO-1's contribution is considerably lower than that of $1\pi_x$, and HOMO-2's contribution is too minimal to be observed in the figure.

IV. DISCUSSION

The numerical accuracy of a TDDFT calculation relies on the choice of the exchange-correlation (XC) functional. An important consideration for simulating strong field processes is that the long-range potential goes to $-1/r$ with r being the electron-ion distance [52]. This is essential for the proper representation of not only the HOMO but the Rydberg orbitals and unbound orbitals that are crucial for a three-step process. LB$_\alpha$ is such a functional [53]. Previous TDDFT calculations using the LB$_\alpha$ functional have reproduced features in HHG spectra observed experimentally, including the Cooper-like minimum in N$_2$ [54] and the isotope effect in H$_2$ [55].

In this study, LB$_\alpha$ modeling yields occupied orbital energies consistent with measured vertical ionization potentials and the permanent dipole moment in agreement with experimental values. The proximity in energies between the HOMO ($1\pi_x$ and $1\pi_y$) and HOMO-1 (5σ) underscores the role of $\psi_j(\boldsymbol{r}, t)$ for these orbitals in dictating the primary contributors to the HHG spectrum. Regarding orbital polarizations, HOMO-1 and HOMO-2 have to be combined for the result to be physically meaningful. The calculated orientation-dependent HHG patterns, primarily influenced by the spatial orientation of molecular dipole moments and molecular orbital properties consistent with experimental values, are unlikely to be significantly affected by minor inaccuracies in the XC functional.

On the other hand, it is important to acknowledge that certain effects, including nonlocal electron exchange-correlation, memory effects, and electron-nuclear correlation, may not be precisely captured or excluded. Should these factors play a substantial role in the HHG of HCN, they might introduce features not accounted for in this study.

V. SUMMARY AND CONCLUSIONS

This study utilizes HCN to explore the dependence of high-order harmonic spectra on the orientation of molecules with significant dipole moments relative to laser polarization.

Our findings, derived from TDDFT calculations, reveal distinct behaviors in the HHG spectra based on molecular orientation. Specifically, even harmonics display the highest intensity at parallel orientation and diminish at perpendicular orientations.

Moreover, we observe that even harmonics exhibit distinct cutoffs compared to odd harmonics. This discrepancy in cutoffs is inconspicuous at parallel orientations but becomes pronounced with increasing angular deviation. As the orientation angle widens, the cutoff for even harmonics decreases while that for odd harmonics remains stable.

Interestingly, even harmonics are also generated perpendicular to the laser polarization, albeit with reduced intensity. Their generation is most pronounced at perpendicular orientation and decreases as the orientation diverges further from the perpendicular.

In contrast, odd harmonics consistently show maximum intensity at perpendicular orientation, aligning with the HOMO being the π orbitals. However, the least intensities for odd harmonics do not occur at parallel orientation but rather at intermediate angles.

Exceptions to these trends are observed near the ionization threshold and the minimum. These variances are subject to the influence of laser parameters on the orientation dependence of the harmonics.

Multiorbital involvement is apparent for HHG of HCN. At any molecular orientation, the HOMOs contribute little to high-order even harmonics. For odd high-order harmonics, the HOMOs' contributions are significant when the orientation angle is at $30°$ or greater.

A notable finding is the presence of a consistent minimum near 22–23 eV, irrespective of laser parameters or molecular orientation, including in purely even spectra perpendicular to the laser polarization. This minimum persists in the spectra of unoriented molecules as well.

[1] G. L. Kamta, A. D. Bandrauk, and P. B. Corkum, J. Phys. B **38**, L339 (2005).

[2] A. Etches and L. B. Madsen, J. Phys. B **43**, 155602 (2010).

[3] H. Li, D. Ray, S. De, I. Znakovskaya, W. Cao, G. Laurent, Z. Wang, M. F. Kling, A. T. Le, and C. L. Cocke, Phys. Rev. A **84**, 043429 (2011).

[4] E. Frumker, N. Kajumba, J. B. Bertrand, H. J. Wörner, C. T. Hebeisen, P. Hockett, M. Spanner, S. Patchkovskii, G. G. Paulus, D. M. Villeneuve, A. Naumov, and P. B. Corkum, Phys. Rev. Lett. **109**, 233904 (2012).

[5] Y. J. Chen, L. B. Fu, and J. Liu, Phys. Rev. Lett. **111**, 073902 (2013).

[6] P. M. Kraus, O. I. Tolstikhin, D. Baykusheva, A. Rupenyan, J. Schneider, C. Z. Bisgaard, T. Morishita, F. Jensen, L. B. Madsen, and H. J. Wörner, Nat. Commun. **6**, 7039 (2015).

[7] S. J. Yu, W. Y. Li, Y. P. Li, and Y. J. Chen, Phys. Rev. A **96**, 013432 (2017).

[8] W. Y. Li, S. J. Yu, S. Wang, and Y. J. Chen, Phys. Rev. A **94**, 053407 (2016).

[9] Y. Ren, L. Jia, Y. Zhang, Z. Zhang, S. Xue, S. Yue, and H. Du, Phys. Rev. A **106**, 033123 (2022).

[10] S. Yu, B. Zhang, Y. Li, S. Yang, and Y. Chen, Phys. Rev. A **90**, 053844 (2014).

[11] F. Mauger, P. M. Abanador, T. D. Scarborough, T. T. Gorman, P. Agostini, L. F. DiMauro, K. Lopata, K. J. Schafer, and M. B. Gaarde, Struct. Dyn. **6**, 044101 (2019).

[12] W. Y. Li, R. H. Xu, X. J. Xie, and Y. J. Chen, Phys. Rev. A **100**, 043421 (2019).

[13] P. M. Kraus, D. Baykusheva, and H. J. Wörner, Phys. Rev. Lett. **113**, 023001 (2014).

[14] P. M. Kraus, B. Mignolet, D. Baykusheva, A. Rupenyan, L. Horný, E. F. Penka, G. Grassi, O. I. Tolstikhin, J. Schneider, F. Jensen, L. B. Madsen, A. D. Bandrauk, F. Remacle, and H. J. Wörner, Science **350**, 790 (2015).

[15] J. L. Krause, K. J. Schafer, and K. C. Kulander, Phys. Rev. A **45**, 4998 (1992).

[16] P. B. Corkum, Phys. Rev. Lett. **71**, 1994 (1993).

[17] H. Stapelfeldt and T. Seideman, Rev. Mod. Phys. **75**, 543 (2003).

[18] K. Lin, I. Tutunnikov, J. Qiang, J. Ma, Q. Song, Q. Ji, W. Zhang, H. Li, F. Sun, X. Gong, H. Li, P. Lu, H. Zeng, Y. Prior, I. S. Averbukh, and J. Wu, Nat. Commun. **9**, 5134 (2018).

[19] C. Jin, S.-J. Wang, X. Zhao, S.-F. Zhao, and C. D. Lin, Phys. Rev. A **101**, 013429 (2020).

[20] A. Rundquist, C. G. Durfee, Z. Chang, C. Herne, S. Backus, M. M. Murnane, and H. C. Kapteyn, Science **280**, 1412 (1998).

[21] C. Jin, B. Li, K. Wang, C. Xu, X. Tang, C. Yu, and C. D. Lin, Phys. Rev. A **102**, 033113 (2020).

[22] T. T. Gorman, T. D. Scarborough, P. M. Abanador, F. Mauger, D. Kiesewetter, P. Sándor, S. Khatri, K. Lopata, K. J. Schafer, P. Agostini, M. B. Gaarde, and L. F. DiMauro, J. Chem. Phys. **150**, 184308 (2019).

[23] H. Hu, N. Li, P. Liu, R. Li, and Z. Xu, Phys. Rev. Lett. **119**, 173201 (2017).

[24] C. Fridh and L. Asbrink, J. Electron Spectrosc. Relat. Phenom. **7**, 119 (1975).

[25] N.-T. Nguyen, B.-V. Tang, and V.-H. Le, J. Mol. Struct. (THEOCHEM) **949**, 52 (2010).

[26] B. K. McFarland, J. P. Farrell, P. H. Bucksbaum, and M. Gühr, Science **322**, 1232 (2008).

[27] O. Smirnova, Y. Mairesse, S. Patchkovskii, N. Dudovich, D. Villeneuve, P. Corkum, and M. Y. Ivanov, Nature (London) **460**, 972 (2009).

[28] A. Ferre, A. E. Boguslavskiy, M. Dagan, V. Blanchet, B. D. Bruner, F. Burgy, A. Camper, D. Descamps, B. Fabre, N. Fedorov, J. Gaudin, G. Geoffroy, J. Mikosch, S. Patchkovskii, S. Petit, T. Ruchon, H. Soifer, D. Staedter, I. Wilkinson, A. Stolow *et al.*, Nat. Commun. **6**, 5952 (2015).

[29] K. A. Hamer, D. R. Tuthill, T. D. Scarborough, L. F. DiMauro, K. Lopata, K. J. Schafer, M. B. Gaarde, and F. Mauger, Phys. Rev. A **104**, 033114 (2021).

[30] Z. Shu, H. Liang, Y. Wang, S. Hu, S. Chen, H. Xu, R. Ma, D. Ding, and J. Chen, Phys. Rev. Lett. **128**, 183202 (2022).

[31] Z. Zhao, J. Yuan, and T. Brabec, Phys. Rev. A **76**, 031404(R) (2007).

[32] S. Patchkovskii, Z. Zhao, T. Brabec, and D. M. Villeneuve, Phys. Rev. Lett. **97**, 123003 (2006).

[33] X. Chu and G. C. Groenenboom, Phys. Rev. A **105**, 053110 (2022).

[34] C. Vozzi, F. Calegari, E. Benedetti, J.-P. Caumes, G. Sansone, S. Stagira, M. Nisoli, R. Torres, E. Heesel, N. Kajumba, J. P. Marangos, C. Altucci, and R. Velotta, Phys. Rev. Lett. **95**, 153902 (2005).

[35] A. T. Le, X. M. Tong, and C. D. Lin, Phys. Rev. A **73**, 041402(R) (2006).

[36] A. J. Uzan, H. Soifer, O. Pedatzur, A. Clergerie, S. Larroque, B. D. Bruner, B. Pons, M. Ivanov, O. Smirnova, and N. Dudovich, Nat. Photon. **14**, 188 (2020).

[37] C. Jin, J. B. Bertrand, R. R. Lucchese, H. J. Worner, P. B. Corkum, D. M. Villeneuve, A.-T. Le, and C. D. Lin, Phys. Rev. A **85**, 013405 (2012).

[38] M. Chini, X. Wang, Y. Cheng, H. Wang, Y. Wu, E. Cunningham, P.-C. Li, J. Heslar, D. A. Telnov, S.-I. Chu, and Z. Chang, Nat. Photon. **8**, 437 (2014).

[39] E. K. U. Gross and W. Kohn, Adv. Quant. Chem. **21**, 255 (1990).

[40] J. Heslar, D. Telnov, and S.-I. Chu, Phys. Rev. A **83**, 043414 (2011).

[41] A. Koushki, J. Mol. Model. **29**, 137 (2023).

[42] X. Chu, Phys. Rev. A **108**, 013116 (2023).

[43] R. van Leeuwen and E. J. Baerends, Phys. Rev. A **49**, 2421 (1994).

[44] X. Chu and M. McIntyre, Phys. Rev. A **83**, 013409 (2011).

[45] X.-M. Tong and S.-I. Chu, Chem. Phys. **217**, 119 (1997).

[46] X. Chu and Shih-I Chu, Phys. Rev. A **63**, 023411 (2001).

[47] G. Herzberg, *Electronic Spectra and Electronic Structure of Polyatomic Molecules* (Van Nostrand, New York, 1966).

[48] C. P. Smyth and K. B. McAlpine, J. Am. Chem. Soc. **56**, 1697 (1934).

[49] D. Frost, S. Lee, and C. McDowell, Chem. Phys. Lett. **23**, 472 (1973).

[50] M. D. Śpiewanowski and L. B. Madsen, Phys. Rev. A **89**, 043407 (2014).

[51] M. Labeye, F. Risoud, C. Lévêque, J. Caillat, A. Maquet, T. Shaaran, P. Salières, and R. Taïeb, Phys. Rev. A **99**, 013412 (2019).

[52] X. Chu and S.-I. Chu, Phys. Rev. A **64**, 063404 (2001).

[53] P. R. T. Schipper, O. V. Gritsenko, S. J. A. van Gisbergen, and E. J. Baerends, J. Chem. Phys. **112**, 1344 (2000).

[54] X. Chu and G. C. Groenenboom, Phys. Rev. A **87**, 013434 (2013).

[55] X. Chu and G. C. Groenenboom, Phys. Rev. A **85**, 053402 (2012).